Visualizing the fractional topological order: From fractional Chern insulators to the Tao-Thouless state

Sutirtha Mukherjee and Kwon Park*
School of Physics, Korea Institute for Advanced Study, Seoul 02455, Korea

(Received 14 June 2023; accepted 7 September 2023; published 25 September 2023)

Strong correlation and topology are two main pillars of modern physics, which can be bridged by fractional quantum Hall states and their lattice analogs known as fractional Chern insulators. A particularly pressing question for fractional Chern insulators is if there exists a lattice analog of the Laughlin state in the 1/3-filled Chern flat band dubbed the Chern-Laughlin state, and if so, how to detect it experimentally. The exact ground state in the 1/3-filled Chern flat band depends on the form of the electron-electron interaction, which can generate various competing ground states derived from, for example, the Laughlin, parafermion, parton, and stripe/nematic states in the 1/3-filled Landau level. In this context, it is of critical importance to precisely identify the exact ground state for a given electron-electron interaction. Here, we propose that the existence of an adiabatic path from the 1/3-filled fractional Chern insulator to the Tao-Thouless state, i.e., the root partition state of the Laughlin state in the thin torus limit, can serve as an effective order parameter for the precise identification of the Chern-Laughlin state. Specifically, by devising a hybrid adiabatic path of first deforming the electron-electron interaction and then taking the thin torus limit, we show that two-dimensional bulk Chern flat bands can host the Chern-Laughlin state at 1/3 filling. More importantly, our results suggest that, unless the electron-electron interaction is strictly of the nearest-neighbor form, the Tao-Thouless state can actually be detected in experiments, for example by using an incommensurate double-walled carbon nanotube made out of the magic-angle twisted bilayer graphene, which allows charge-sensitive surface measurements such as scanning tunneling microscopy. This method can be extended to various other fractional Chern insulators corresponding to both Abelian and non-Abelian fractional quantum Hall states.

DOI: 10.1103/PhysRevResearch.5.033212

I. INTRODUCTION

Ordered phases of matter are often characterized by spontaneous symmetry breaking. The ferromagnet is a well-known example in this class of ordered phases, characterized by spontaneous breaking of spin rotational symmetry. Topological insulators belong to a different class of ordered phases, characterized by topology. Specifically, Chern insulators are characterized by the topological invariant defined for noninteracting energy bands, called the Chern number. Chern insulators are the lattice analog of weakly correlated integer quantum Hall states (IQHSs) occurring in fully filled Landau levels (LLs). Topological insulators are two independent copies of Chern insulators with opposite Chern numbers, which are typically protected by time-reversal symmetry.

Meanwhile, there is yet another class of ordered phases, which cannot be characterized by either spontaneous symmetry breaking or noninteracting topological invariants. Occurring in fractionally filled LLs, fractional quantum Hall states (FQHSs) [1] are a quintessential example in this class of ordered phases, induced by the intricate interplay between strong correlation and topology. Fractional Chern insulators (FCIs) are envisioned as a lattice analog of FQHSs [2–15], arising in sufficiently flat energy bands with nontrivial Chern numbers, called Chern flat bands, where the electron-electron interaction dominates the band dispersion. In the absence of conventional order parameters, it is important to know exactly how to characterize FCIs and, for that matter, strongly correlated topological phases in general.

Immediately after the discovery of the Laughlin state [16], there were several theoretical attempts [17,18] to devise an order parameter for the characterization of FQHSs by drawing an analogy with the Bose-Einstein condensate. Eventually, FQHSs became better understood in terms of the composite fermion (CF) theory [19], according to which FQHSs are emergent IQHSs occurring in fully filled effective LLs formed by CFs. Unfortunately, it is still not known how to compute the Chern number for such effective LLs.

An alternative method, which can also be applied to FCIs [4,5], is to compute the many-body Chern number [20] for the ground-state manifold (GSM) with a certain distinctive topological degeneracy under the periodic boundary condition. The GSM is accompanied by level crossing between degenerate ground states as a function of flux insertion [21], which we call topological spectral flow in this work. For example, the Laughlin state generates the GSM with a triple

*kpark@kias.re.kr

topological degeneracy in torus geometry. When computed for the entire GSM of the Laughlin state, the total many-body Chern number is simply unity [4,20]. Considering that the GSM is supposed to be exactly degenerate in the thermodynamic limit, the Chern number for each individual copy of the Laughlin state can be regarded as $1/3$, which is simply equal to the filling factor, or the Hall conductance in units of the conductance quantum.

In fact, as a general rule, the ratio between the total many-body Chern number and the topological degeneracy is always equal to the filling factor. This means that, for a given filling factor, the topological degeneracy completely determines the many-body Chern number. Consequently, the topological degeneracy can serve as an effective order parameter for the characterization of FQHSs.

Moreover, the topological degeneracy can be used to distinguish between various competing ground states occurring at the same filling factor. Specifically, the $1/3$-filled Chern flat band can host various competing ground states derived from, for example, the Laughlin [16], parafermion [22], parton [23], and stripe/nematic [24–26] states via the one-to-one mapping between FQHSs and FCIs [6,9]. Out of these four competing ground states, the Laughlin, parafermion, and parton states are incompressible, with each state expected to have its own distinctive topological degeneracy with a clear energy gap [22]. On the other hand, the stripe/nematic state is compressible, in which case the GSM is not properly defined due to the absence of the energy gap.

It is, however, very difficult for the topological degeneracy to become an experimentally viable order parameter. The problem is that the topological degeneracy can manifest itself only in torus geometry with a hypothetical periodic boundary condition. Meanwhile, incompressible ground states are always uniquely determined in disk geometry with a realistic open boundary condition. Will there be any experimentally viable method to manifest the topological degeneracy? In this work, we propose such a method.

Our method is based on the fact that FQHSs evolve adiabatically to so-called root partition states in the thin torus limit [27–31], which, as far as the charge degree of freedom is concerned, are nothing but simple charge density wave (CDW) states induced by the suppression of quantum fluctuations. For example, the Laughlin state evolves adiabatically to the Tao-Thouless state in the thin torus limit [27], which is composed of three simple CDW states represented by $|100\cdots\rangle$, $|010\cdots\rangle$, and $|001\cdots\rangle$, with 1 and 0 denoting filled and empty LL eigenstates, respectively, and ellipses denoting repeated patterns. The actual ground state is supposed to be one of these three CDW states randomly selected by spontaneous breaking of the translational symmetry due to the open boundary condition and/or charge-pinning impurities. In addition to the topological degeneracy, root partition states are also useful to understand other key characteristics of FQHSs, such as the entanglement spectrum [32–37]. Metaphorically, root partition states are the "DNA" of FQHSs.

Despite their significance, however, root partition states have not been studied thoroughly for various reasons. One of the main reasons is that torus geometry is impossible to realize in conventional experimental setup for FQHSs, where the two-dimensional (2D) electron gas cannot be bent to form a toroidal or tubular surface. One may raise an objection to this assessment by arguing that FQHSs have been obtained in graphene, which can be made into a carbon nanotube. Despite the nominal tubular shape, however, there remains a serious problem preventing the realization of the thin torus limit for FQHSs in carbon nanotubes. That is, magnetic fields cannot be applied radially so that they pierce the surface of carbon nanotubes from inside out or vice versa.

Fortunately, no magnetic fields need to be applied for FCIs since Chern flat bands are already topologically nontrivial by themselves. In this regard, recently observed FCIs [15] in magic-angle twisted bilayer graphene (MATBG) [38,39] can provide a perfect opportunity for the experimental detection of root partition states and thus a clear visualization of the fractional topological order. Specifically, root partition states can actually be detected in an incommensurate double-walled carbon nanotube [40] made out of the MATBG, which allows charge-sensitive surface measurements such as scanning tunneling microscopy [41,42]. A detection of the Tao-Thouless state can be taken as conclusive evidence of the true existence of the Chern-Laughlin state.

As mentioned previously, however, the existence of the Chern-Laughlin state is not always guaranteed in the $1/3$-filled Chern flat band since the exact ground state depends on the form of the electron-electron interaction, competing against various states. In this work, we devise a hybrid adiabatic path of first deforming the electron-electron interaction and then taking the thin torus limit to show that the exact ground state in $1/3$-filled Chern flat bands with not only Coulomb but also nearest-neighbor interactions can indeed evolve adiabatically to the Tao-Thouless state in the thin torus limit. More importantly, our results suggest that, unless the electron-electron interaction is strictly of the nearest-neighbor form, the Tao-Thouless state can actually be realized in the thin torus limit of Chern flat bands.

With the incorporation of appropriate quantum fluctuations, the Tao-Thouless state can be transformed into the Chern-Laughlin state, which is shown to have high overlaps with the exact ground states of both Coulomb and nearest-neighbor interactions in the 2D bulk of the $1/3$-filled Chern flat band. Note that our results are consistent with previous results obtained for the nearest-neighbor interaction [9]. In conclusion, the existence of an adiabatic path from the $1/3$-filled FCI to the Tao-Thouless state can serve as an effective order parameter for the precise identification of the Chern-Laughlin state both theoretically and experimentally.

The rest of this paper is organized as follows. In Sec. II, we provide details of the microscopic model Hamiltonians for strongly correlated Chern flat bands. Specifically, we focus on two microscopic models: (i) the checkerboard lattice model [2] and (ii) the kagome lattice model [3]. In Secs. III and IV, we present our main results obtained via exact diagonalization of these two models, respectively.

Concretely, in Secs. III A and IV A, we construct the hybrid adiabatic path from the $1/3$-filled FCI to the Tao-Thouless state by first deforming the electron-electron interaction and then taking the thin torus limit. In Secs. III B and IV B, we study the topological spectral flow of the triply degenerate GSM for the $1/3$-filled FCI as a function of the flux insertion. In Secs. III C and IV C, we check if the many-body

Chern number is correctly obtained for the 1/3-filled FCI. In Secs. III D and IV D, we construct the topological basis, which can be used to represent not only the Tao-Thouless state in the thin torus limit, but also the Chern-Laughlin state after the incorporation of appropriate quantum fluctuations. In Secs. III E and IV E, we compute the overlap between the 1/3-filled FCI and the Tao-Thouless state as a function of the aspect ratio. In Secs. III F and IV F, we compute the overlap between the 1/3-filled FCI and the Chern-Laughlin state at each aspect ratio. Finally, we conclude in Sec. V by discussing the possible application of our method to various other FCIs corresponding to both Abelian and non-Abelian FQHSs.

II. HAMILTONIAN

We begin by considering a generic form of the microscopic model Hamiltonian for strongly correlated Chern flat bands:

$$H = H_0 + H_{\text{int}} = \sum_{\alpha,\mathbf{k}} \epsilon_{\alpha\mathbf{k}} c^\dagger_{\alpha\mathbf{k}} c_{\alpha\mathbf{k}} + \sum_{i<j} U_{ij} n_i n_j, \tag{1}$$

where H_0 and H_{int} denote the kinetic and interaction parts of the microscopic model Hamiltonian, respectively.

The band dispersion, $\epsilon_{\alpha\mathbf{k}}$, is given as a function of the band index α and the Bloch momentum $\mathbf{k}$. Depending on the choice of system parameters, some energy bands can be both topologically nontrivial and nearly flat, i.e., Chern flat bands. Here, we focus on two tight-binding model Hamiltonians for H_0 with one in the checkerboard lattice [2] and the other in the kagome lattice [3]. For simplicity, we relegate the technical details of these two tight-binding model Hamiltonians to Appendix A.

We have chosen the aforementioned tight-biding models since there are only two and three sites per unit cell in the checkerboard and kagome lattice models, respectively. Note that exact diagonalization cannot be directly performed in the fully microscopic Hamiltonian of the MATBG due to the large number of carbon atoms ($\sim$13 000 C) per moiré unit cell [39]. Meanwhile, some faithful tight-binding models have recently been proposed for the MATBG at the expense of having multiple bands up to 10 [43]. For future work, it would be interesting to apply our method to such tight-biding models.

The electron-electron interaction, U_{ij}, is initially taken as the nearest-neighbor interaction, U^{NN}_{ij}, but later extended to the Coulomb interaction, U^{Coul}_{ij}, for reasons explained later. Actually, in this work, we consider a generalized electron-electron interaction, $U_{ij}(\lambda)$, to construct the hybrid adiabatic path from FCIs to the Tao-Thouless state:

$$U_{ij}(\lambda) = (1-\lambda)U^{\text{NN}}_{ij} + \lambda U^{\text{Coul}}_{ij}, \tag{2}$$

where λ is the mixing parameter tuning the range of interaction.

The final Hamiltonian of interest is the Chern-flat-band-projected Hamiltonian,

$$\mathcal{H}_{\text{CFB}} = \mathcal{P}_{\text{CFB}} H \mathcal{P}_{\text{CFB}}, \tag{3}$$

where $\mathcal{P}_{\text{CFB}}$ is the projection operator to a certain desired Chern flat band. After the Chern-flat-band projection, the band dispersion is dominated by the electron-electron interaction, whose matrix elements are provided in Appendix B.

It is, however, important to note that Chern flat bands are not strictly flat. In contrast to the usual practice in the community, here we keep the band dispersion as it is, which turns out to be crucial in the thin torus limit, as shown below.

III. RESULTS FOR THE CHECKERBOARD LATTICE MODEL

In this section, we analyze $\mathcal{H}_{\text{CFB}}$ via exact diagonalization for the checkerboard lattice model at 1/3 filling.

A. Hybrid adiabatic path

We begin by checking what happens to energy spectra if one takes the thin torus limit directly in Chern flat bands with the nearest-neighbor interaction, $U^{\text{NN}}_{ij} = U\delta_{\langle i,j\rangle}$. Throughout this work, we set $U = t$, with t being the nearest-neighbor hopping amplitude in the checkerboard lattice model.

The thin torus limit is achieved by increasing the aspect ratio of the system, r_a, while fixing the total number of sites, N_s, and that of electrons, N. Specifically, we consider the $N_x \times N_y$ rectangular supercell, whose lattice points are composed of primitive unit cells of the checkerboard lattice with two sites. In this case, $r_a = N_x/N_y$ and $N_s = N_xN_y$. Also, $N_s = 3N$ at 1/3 filling.

Figures 1(a)–1(d) show energy spectra of the nearest-neighbor interaction in the checkerboard lattice model as a function of (N_x, N_y) for $N = 8$ and $N_s = 24$. As one can see, the triply degenerate GSM persists up to $(N_x, N_y) = (12, 2)$, but collapses at $(N_x, N_y) = (24, 1)$. The GSM collapses since the energy gap induced by the nearest-neighbor interaction becomes exceedingly small even when the band dispersion is completely ignored [44]. Such a small energy gap can be easily wiped out by nearly, but not entirely, flat band dispersions.

To establish an adiabatic path from the 1/3-filled FCI to the Tao-Thouless state, it is necessary to find the right form of the electron-electron interaction that can sustain the energy gap in the entire process of taking the thin torus limit. To this end, we consider the Coulomb interaction, which can be written in the checkerboard lattice as follows:

$$U^{\text{Coul}}_{ij} = \frac{e^2}{\epsilon} \sum_{l_1,l_2} \frac{1}{|\mathbf{r}_{ij} + l_1 N_x \hat{x} + l_2 N_y \hat{y}|}, \tag{4}$$

where $\mathbf{r}_{ij}$ is the relative position vector between the ith and jth sites within the boundary of a supercell. For convenience, unless stated otherwise, we set all lattice constants to be unity, i.e., $a_x = a_y = 1$, with a_x and a_y being the lattice constants in the x and y directions, respectively. Also, throughout this work, we set $e^2/\epsilon = t$, with t being the nearest-neighbor hopping amplitude in the checkerboard lattice model. For other lattices with nonrectangular supercells such as the kagome lattice, $\hat{x}$ and $\hat{y}$ should be replaced by the primitive lattice vectors, $\hat{e}_1$ and $\hat{e}_2$, corresponding to the lattice structure of supercells.

It is important to note that the Coulomb interaction in Eq. (4) includes all long-range contributions from infinitely repeated image charges induced by the periodic boundary condition [45]. As is well known, the summation of such long-range contributions converges very slowly so that special care

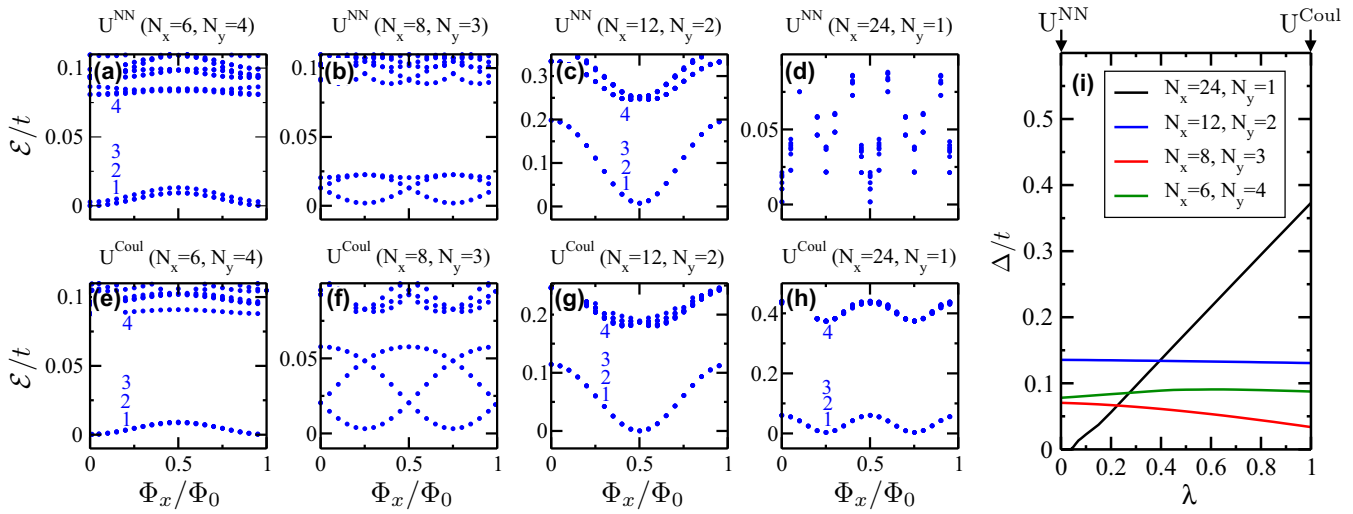

FIG. 1. Energy spectra of the nearest-neighbor and Coulomb interactions in the checkerboard lattice model. (a)–(d) Energy spectra of the nearest-neighbor interaction, U^{NN}, in the checkerboard lattice model as a function of the test flux along the x direction, Φ_x/Φ_0, for various values of (N_x, N_y). Φ_0 is the magnetic flux quantum. (e)–(h) Similar energy spectra of the Coulomb interaction, U^{Coul}. Here, the numbers of electrons and sites are $N = 8$ and $N_s = N_x N_y = 24$, respectively. Energies, $\mathcal{E}$, are given in units of the nearest-neighbor hopping amplitude, t, and offset by the lowest energy in each panel. The first four lowest energies are specified by numbers when three copies of the ground state have almost the same energy. (i) Energy gap, Δ, between the third and fourth lowest energies as a function of the mixing parameter, λ, tuning the range of interaction via $U(\lambda) = (1-\lambda)U^{\mathrm{NN}} + \lambda U^{\mathrm{Coul}}$. Here, Φ_x is set to be zero.

must be taken. Here, we use the Ewald summation technique [46]. See Appendix C for details.

Figures 1(e)–1(h) show energy spectra of the Coulomb interaction in the checkerboard lattice model. As one can see, the triply degenerate GSM remains robust all the way to the thin torus limit. This shows that the long-range nature of the Coulomb interaction is important to stabilize the adiabatic path to the Tao-Thouless state. It is interesting to mention that the triply degenerate GSM can survive also for the screened Coulomb interaction, which is represented via the Yukawa potential.

Motivated by this finding, we devise a hybrid adiabatic path connecting between the 1/3-filled FCI in the 2D bulk and the Tao-Thouless state in the thin torus limit. Our path is composed of two pieces: (i) deforming the electron-electron interaction from the nearest-neighbor to Coulomb interaction in the 2D bulk, and (ii) taking the thin torus limit with the Coulomb interaction. This path becomes entirely adiabatic if the first piece of the path is adiabatic since the second is already shown to be so.

To this end, we check if the triply degenerate GSM can survive during the deformation process of the electron-electron interaction via $U(\lambda) = (1-\lambda)U^{\mathrm{NN}} + \lambda U^{\mathrm{Coul}}$ with $\lambda \in [0, 1]$. Figure 1(i) shows that the energy gap between the third and fourth lowest energies (which separates the triply degenerate GSM and excited states) remains open as a function of λ in the 2D bulk, i.e., $(N_x, N_y) = (6, 4)$. Actually, the energy gap only closes at very small λ in the thin torus limit, i.e., $(N_x, N_y) = (24, 1)$. This means that the Tao-Thouless state can actually be obtained in the thin torus limit unless the electron-electron interaction is strictly of the nearest-neighbor form.

Having established that the triply degenerate GSM can survive along the hybrid adiabatic path, we next check if the triply degenerate GSM satisfies two topological properties, which should be so if it were indeed the Laughlin state. Specifically, in Sec. III B, we investigate the spectral flow of the triply degenerate GSM as a function of the test flux to check if three constituent ground states interchange between themselves after the 2π insertion of the test flux. Also, in Sec. III C, we compute the many-body Chern number of the triply degenerate GSM to check if it is unity as a whole.

B. Topological spectral flow

One of the most important topological properties of the Laughlin state is that there exists a peculiar spectral flow of the triply degenerate GSM so that three constituent ground states interchange between themselves after the 2π insertion of the test flux. As mentioned previously, let us call such a spectral flow the topological spectral flow.

First, as shown in Figs. 1(b) and 1(f), the topological spectral flow can be clearly verified at $(N_x, N_y) = (8, 3)$, where all three constituent ground states of the triply degenerate GSM occur in the same K_x, but different K_y, sectors, with K_x and K_y being the total momenta along the x and y directions, respectively. Note that, generally, three constituent ground states occur in the same K_x, but different K_y sectors if N_y is a multiple of 3. Considering that the flux insertion along the x direction shifts K_y, it is natural to expect that the topological spectral flow exists at this aspect ratio of $(N_x, N_y) = (8, 3)$, which indeed turns out to be the case. Unfortunately, however, it is not easy to verify the topological spectral flow at other aspect ratios, where all three ground-state energies of the triply degenerate GSM fall almost exactly on top of each other.

To overcome this problem, we realize that N_x is a multiple of 3 at all the other aspect ratios, and therefore three constituent ground states of the triply degenerate GSM occur in

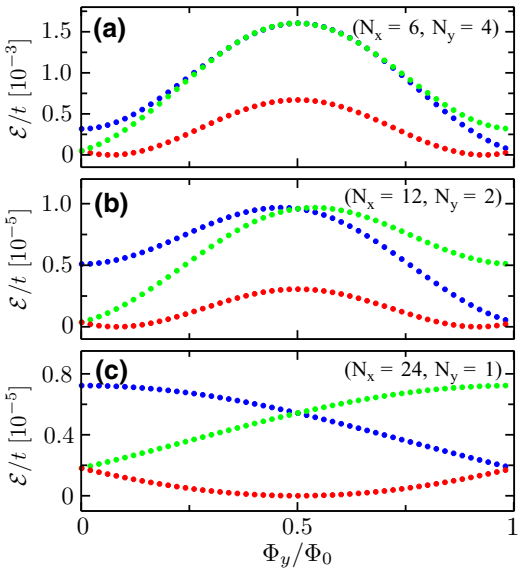

FIG. 2. Topological spectral flow of the triply degenerate ground-state manifold (GSM) under the flux insertion along the y direction in the checkerboard lattice model. Three ground-state energies of the triply degenerate GSM for the Coulomb interaction are plotted as a function of the test flux along the y direction, Φ_y/Φ_0, for $(N_x, N_y) = (6, 4)$, $(12, 2)$, and $(24, 1)$ in (a), (b), and (c), respectively. Ground-state energies, $\mathcal{E}$, are given in units of the nearest-neighbor hopping amplitude, t, and offset by the lowest energy in each panel. Different colors (red, green, and blue) denote that each ground state of the triply degenerate GSM belongs to a different sector of the total momentum along the x direction.

the same K_y, but different K_x, sectors, which is exactly opposite to what happens at $(N_x, N_y) = (8, 3)$. In this situation, it is natural to shift K_x by inserting the test flux along the y direction. As expected, Fig. 2 shows that the topological spectral flow exists as a function of the test flux along the y direction for $(N_x, N_y) = (6, 4)$, $(12, 2)$, and $(24, 1)$. Note that, at these aspect ratios, the energy differences between three constituent ground states of the triply degenerate GSM are exceedingly small in comparison with those at $(N_x, N_y) = (8, 3)$.

C. Many-body Chern number

Now, we check if the many-body Chern number is correctly obtained for the triply degenerate GSM of the Coulomb interaction at all aspect ratios. Note that the many-body Chern number has been previously computed for the nearest- and next-nearest-neighbor interactions at an aspect ratio corresponding to the 2D bulk [4].

Simply put, the many-body Chern number is the total Berry flux piercing through the parameter space of the twist angle under the twisted boundary condition. Concretely, the many-body Chern number can be defined as follows:

$$\mathcal{C}_{\mathrm{MB}} = \frac{1}{2\pi}\int_0^{2\pi} d\theta_x \int_0^{2\pi} d\theta_y F(\theta_x, \theta_y), \tag{5}$$

where θ_x and θ_y are the twist angles in x and y directions, respectively, and $F(\theta_x, \theta_y)$ is the corresponding many-body Berry curvature,

$$F(\theta_x, \theta_y) = \frac{\partial A_y}{\partial \theta_x} - \frac{\partial A_x}{\partial \theta_y}, \tag{6}$$

where $A_{j=x,y}$ is the many-body Berry connection,

$$A_j = \langle \Psi(\theta_x, \theta_y) | i \frac{\partial}{\partial \theta_j} | \Psi(\theta_x, \theta_y) \rangle, \tag{7}$$

with $\Psi(\theta_x, \theta_y)$ being the exact ground-state wave function at θ_x and θ_y.

For the actual numerical computation of C_{MB}, the integral in Eq. (5) is transformed into a finite sum by discretizing the parameter space of θ_x and θ_y. This can be implemented via an efficient method [47,48] allowing the accurate computation of the Chern number with only about 100 discretized bins.

Consequently, we have confirmed that the total many-body Chern number for the entire triply degenerate GSM is precisely quantized to be unity for all possible aspect ratios with $N = 8$ and $N_s = 24$. While not completely legitimate, the many-body Chern number can also be evaluated for each constituent ground state of the triply degenerate GSM, which turns out to be very close to $1/3$, as expected.

Next, we check if each constituent ground state of the triply degenerate GSM actually reduces to the Tao-Thouless state in the thin torus limit. To this end, it is important to choose the appropriate topological basis representing the Tao-Thouless state and also FCIs in the presence of full quantum fluctuations.

D. Wannier-Stark ladder eigenstates

The topological basis to represent FCIs is typically constructed in terms of maximallylocalized hybrid Wannier functions [6], which can be mapped one-to-one to LL eigenstates in the Landau gauge. In this work, we use essentially the same topological basis but with a different method of construction that facilitates a much more intuitive implementation of the periodic boundary condition in finite-size Chern flat bands than the previous approach [9].

We begin by noticing that maximally localized hybrid Wannier functions can actually be understood as Wannier-Stark ladder (WSL) eigenstates [49–55] formed in the Chern flat band under an effective electric field [56]. Specifically, WSL eigenstates are the energy eigenstates of the Stark Hamiltonian:

$$\mathcal{H}_{\mathrm{Stark}} \phi^{\mathrm{WSL}} = \mathcal{E}_{\mathrm{WSL}} \phi^{\mathrm{WSL}} \tag{8}$$

with

$$\mathcal{H}_{\mathrm{Stark}} = \epsilon_{\mathbf{k}} + e\mathbf{E} \cdot (i\nabla_{\mathbf{k}} + \mathcal{A}_{\mathbf{k}}), \tag{9}$$

where $\epsilon_{\mathbf{k}}$ is the energy dispersion of the Chern flat band, $\mathbf{E}$ is the effective electric field tuning the wave-packet localization width of WSL eigenstates, and $\mathcal{A}_{\mathbf{k}} = \langle u_{\mathbf{k}} | i\nabla_{\mathbf{k}} | u_{\mathbf{k}} \rangle$ is the Berry connection of Bloch states. It is important to note that the effective electric field is only needed to generate WSL eigenstates, which form an alternative basis set replacing the usual one formed by Bloch states. Eventually, our objective is to diagonalize $\mathcal{H}_{\mathrm{CFB}}$ by using WSL eigenstates as basis states.

The energy eigenvalue of WSL eigenstates is given by

$$\mathcal{E}_{\mathrm{WSL}} = \bar{\epsilon}(k_\perp) + \Omega(n + \gamma^{\mathrm{Zak}}(k_\perp)/2\pi), \tag{10}$$

where $k_\perp$ is the momentum perpendicular to $\mathbf{E}$, and $\Omega = eEa_\parallel$ is the Bloch frequency, with E and $a_\parallel$ being the strength of $\mathbf{E}$ and the lattice constant parallel to $\mathbf{E}$, respectively. Likewise, $k_\parallel$ is the momentum parallel to $\mathbf{E}$, and $a_\perp$ is the lattice constant perpendicular to $\mathbf{E}$. As one can see, $\mathcal{E}_{\rm WSL}$ is composed of three terms: (i) the $k_\parallel$-averaged band energy at a fixed $k_\perp$,

$$\bar{\epsilon}(k_\perp) = \frac{a_\parallel}{2\pi} \oint dk_\parallel \epsilon_{\mathbf{k}}, \tag{11}$$

(ii) an integer called the WSL index, n, and (iii) the Zak phase [57],

$$\gamma^{\rm Zak}(k_\perp) = \oint d\mathbf{k}_\parallel \cdot \mathcal{A}_{\mathbf{k}}, \tag{12}$$

which contains the topological information of the Chern flat band as explained below. Note that the Zak phase is also known as the polarization [58].

Note that $\phi^{\rm WSL}$ is given as a function of $k_\parallel$ as follows:

$$\phi^{\rm WSL}_{n,k_\perp}(k_\parallel) = e^{-\frac{i}{\Omega}\int_0^{k_\parallel} dk'_\parallel [\mathcal{E}_{\rm WSL} - \epsilon_{\mathbf{k}'} - \Omega \hat{e}_\parallel \cdot \mathcal{A}_{\mathbf{k}'}]}, \tag{13}$$

where $\mathbf{k}' = k'_\parallel \hat{e}_\parallel + k_\perp \hat{e}_\perp$, with $\hat{e}_\parallel$ and $\hat{e}_\perp$ being the unit vectors parallel and perpendicular to $\mathbf{E}$, respectively. Maximally localized hybrid Wannier functions are obtained as the Fourier transform of $\phi^{\rm WSL}_{n,k_\perp}(k_\parallel)$ with respect to $k_\parallel$ in the limit of infinitely large Ω, where the effects of the band dispersion can be completely ignored. As mentioned above, in this work we treat Ω as a variational parameter to tune the wave-packet localization width of WSL eigenstates.

The topological information of the Chern band is contained in the Zak phase via the winding number of WSL eigenstates [56]. Specifically, the wave-packet center position of WSL eigenstates can be computed as the expectation value of the *gauge-invariant* position operator along the effective electric field:

$$\begin{aligned}\langle \mathbf{r} \rangle \cdot \hat{e}_\parallel / a_\parallel &= \left\langle \phi^{\rm WSL}_{n,k_\perp}(k_\parallel) \middle| i\frac{\partial}{\partial k_\parallel} + \mathcal{A}_{\mathbf{k}} \cdot \hat{e}_\parallel \middle| \phi^{\rm WSL}_{n,k_\perp}(k_\parallel) \right\rangle \\ &= n + \gamma^{\rm Zak}(k_\perp)/2\pi, \end{aligned} \tag{14}$$

which can move up or down by one unit as $\gamma^{\rm Zak}(k_\perp)$ acquires an integer multiple of 2π after $k_\perp$ sweeps across the Brillouin zone in the Chern band. Mathematically, the Chern number, $\mathcal{C}$, is related with the Zak phase as follows:

$$\mathcal{C} = \frac{1}{2\pi}[\gamma^{\rm Zak}(2\pi) - \gamma^{\rm Zak}(0)], \tag{15}$$

which measures the winding number of WSL eigenstates. It is worthwhile to mention that the gauge-invariant position operator generates essentially identical results to those obtained by using Resta's formula [59].

Despite the aforementioned various nice properties of WSL eigenstates, however, there is a technical problem in imposing the periodic boundary condition to WSL eigenstates in finite-size Chern flat bands, where exact diagonalization should be actually performed. In fact, the same problem exists for LL eigenstates in finite-size LLs. Fortunately, this problem can be solved in finite-size LLs by using elliptic theta functions [60]. Motivated by this solution, a similar technique has been developed for maximally localized hybrid Wannier functions [9].

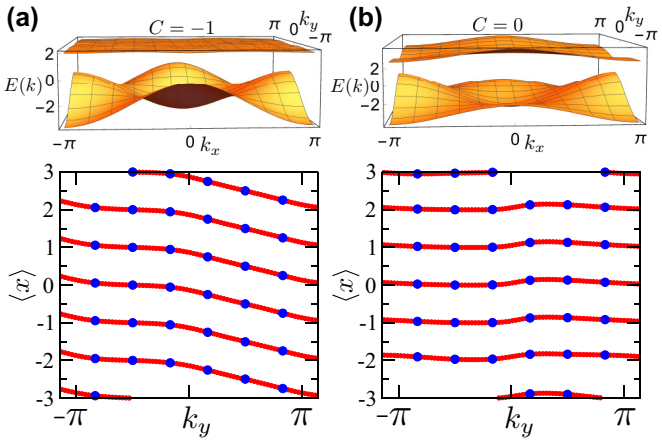

FIG. 3. Topological winding of Wannier-Stark ladder (WSL) eigenstates in the checkerboard lattice model. The effective electric field inducing WSL eigenstates is applied along the x direction. (a) Wave-packet center position $\langle x \rangle$ of WSL eigenstates as a function of the momentum along the y direction, k_y, in the Chern flat band of the checkerboard lattice model, which is the upper energy band indicated by the Chern number $\mathcal{C} = -1$ in the top panel. Topological winding with a negative slope confirms $\mathcal{C} = -1$. (b) Similar plot in the topologically trivial situation, where all energy bands are topologically trivial with $\mathcal{C} = 0$. As one can see, there is no winding. Blue dots represent wave-packet center positions obtained at zero test flux, which are shifted along red lines with an insertion of the test flux. Here, $(N_x, N_y) = (6, 6)$.

In this work, we use a different approach, where the periodic boundary condition can be imposed to WSL eigenstates in a more intuitive way. Our approach is based on the fact that WSL eigenstates can be periodized by discretizing momenta in the Stark Hamiltonian, $\mathcal{H}_{\rm Stark}$, in Eq. (9). Concretely, $\mathcal{H}_{\rm Stark}$ can be discretized by setting $[\epsilon_{\mathbf{k}}]_{\mathbf{k}_1\mathbf{k}_2} = \epsilon_{\mathbf{k}_1}\delta_{\mathbf{k}_1\mathbf{k}_2}$ and $[\mathcal{A}_{\mathbf{k}}]_{\mathbf{k}_1\mathbf{k}_2} = \mathcal{A}_{\mathbf{k}_1}\delta_{\mathbf{k}_1\mathbf{k}_2}$, where $\delta_{\mathbf{k}_1\mathbf{k}_2}$ is the usual Kronecker delta with discrete momenta. Meanwhile, the momentum differentiation, or the canonical position operator, is replaced by $[\hat{\mathcal{R}}]_{\mathbf{k}_1\mathbf{k}_2} \equiv \langle \mathbf{k}_1 | i\nabla_{\mathbf{k}} | \mathbf{k}_2 \rangle = i\nabla_{\mathbf{k}_1}\delta_{\rm D}(\mathbf{k}_1 - \mathbf{k}_2)$, where $\delta_{\rm D}(\mathbf{k}_1 - \mathbf{k}_2)$ is the discretized delta function defined as the Dirichlet kernel [61]. Periodized WSL eigenstates can be obtained by simply diagonalizing the so-discretized Stark Hamiltonian.

Figure 3(a) shows the topological winding of WSL eigenstates in the Chern flat band of the checkerboard lattice model with $(N_x, N_y) = (6, 6)$. With the Chern number $\mathcal{C} = -1$, here, the wave-packet center position of WSL eigenstates winds down monotonically as a function of $k_\perp = k_y$ in the presence of the effective electric field applied along the x direction. By contrast, Fig. 3(b) shows that there is no such winding in the topologically trivial situation. This reveals that there is a strong similarity between LL eigenstates in the lowest LL and WSL eigenstates in the Chern flat band. Specifically, the wave-packet center position of LL eigenstates increases or decreases linearly as a function of $k_{\rm LL}$, with $k_{\rm LL}$ being the momentum of LL eigenstates in the Landau gauge. Considering that the wave-packet center position of WSL eigenstates also increases or decreases monotonically as a function of unfolded $k_\perp$, i.e., $k_\perp + 2\pi n$, one can establish a one-to-one mapping between LL and WSL eigenstates via $k_{\rm LL} \leftrightarrow k_\perp + 2\pi n$.

Interestingly, this one-to-one mapping can explain why strongly nonuniform Berry curvatures could hinder the emergence of FCIs. For the one-to-one mapping between LL and WSL eigenstates to work properly, the wave-packet center positions should be as equally spaced as possible. Technically, this can be achieved if the Zak phase, $\gamma^{\rm Zak}$, follows a linear function of $k_\perp$, which can be obtained in the presence of a uniform Berry curvature. While Chern bands can be made flat in energy, the Berry curvature is generally rather nonuniform. Fortunately, as shown in Fig. 3(a), the wave-packet center positions of WSL eigenstates are more or less equally spaced, making the one-to-one mapping between LL and WSL eigenstates quite effective.

As mentioned previously, our objective is to diagonalize $\mathcal{H}_{\rm CFB}$ by using periodized WSL eigenstates as basis states rather than Bloch states. Of course, this change of basis does not affect any physical observables so that all energy spectra in Figs. 1 and 2 remain exactly the same as before. An advantage of using WSL eigenstates as basis states is that each eigenstate of $\mathcal{H}_{\rm CFB}$ can now be directly compared with the corresponding FQHS via the one-to-one mapping between LL and WSL eigenstates. Particularly, we can now compute the overlap between three exact ground states of the triply degenerate GSM for the Coulomb interaction and the Tao-Thouless state as a function of the aspect ratio to check if the 1/3-filled FCI indeed evolves into the Tao-Thouless state in the thin torus limit. Note that the Tao-Thouless state can be written as $|100\cdots\rangle$, $|010\cdots\rangle$, and $|001\cdots\rangle$ in terms of both LL and WSL eigenstates.

E. Tao-Thouless state

Let us begin by estimating when the Tao-Thouless state is expected to occur as a function of the aspect ratio. To this end, it is necessary to understand why root partition states are formed for FQHSs in the first place. Let L_x and L_y be the lengths of the torus along longer and shorter directions, respectively. Note that the total surface area of the torus, $A = L_x L_y$, is fixed for a given filling factor, ν, with a fixed number of electrons, N, via $A = 2\pi l_B^2 N/\nu$, with l_B being the magnetic length. For FQHSs, root partition states start to form when two adjacent wave packets of LL eigenstates become sufficiently well separated in comparison with their localization width so that quantum fluctuations are suppressed. Specifically, this happens at $L_y \lesssim 2\pi l_B$, corresponding to the aspect ratio $r_a = L_x/L_y \gtrsim N/2\pi\nu$.

Now, an important question is if the Tao-Thouless state occurs at the similar aspect ratio for FCIs. To answer this question, we compute the *degeneracy-averaged* square of overlap [9] between three exact ground states of the triply degenerate GSM for the Coulomb interaction, $|\Psi^{\rm Coul}_{n=1,2,3}\rangle$, and the Tao-Thouless state, $|\Psi^{\rm TT}_{n=1,2,3}\rangle$, as a function of the aspect ratio $r_a = N_x/N_y$:

$$O^2_{\rm TT} = \frac{1}{3}\sum_{n,m=1}^{3} \left|\langle \Psi^{\rm TT}_n | \Psi^{\rm Coul}_m\rangle\right|^2, \tag{16}$$

which can be compared with the similar overlap for FQHSs. Note that here, the wave-packet localization width of WSL eigenstates is set to zero by taking the limit of large effective electric fields, in which case WSL eigenstates are simply equal to maximally localized hybrid Wannier functions. We investigate later what happens at finite electric fields.

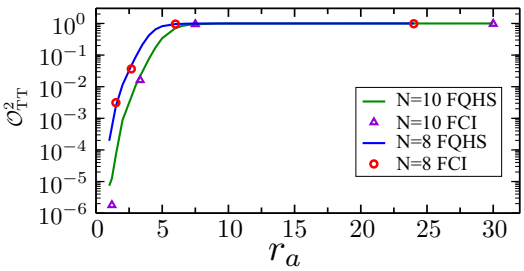

FIG. 4. Overlap between the 1/3-filled fractional Chern insulator (FCI) and the Tao-Thouless state in the checkerboard lattice model. Open symbols denote the degeneracy-averaged square of overlap between three exact ground states of the triply degenerate GSM for the Coulomb interaction and the Tao-Thouless state, $O^2_{\rm TT}$, in the 1/3-filled Chern flat band of the checkerboard lattice model as a function of $r_a = N_x/N_y$. Specifically, circles and triangles indicate $O^2_{\rm TT}$ as a function of r_a for two different electron numbers, $N = 8$ and 10, respectively. Continuous lines denote similar overlaps for the 1/3-filled fractional quantum Hall state (FQHS).

Figure 4 shows that $O^2_{\rm TT}$ follows almost exactly the same curve of the similar overlap for the 1/3-filled FQHS, becoming essentially unity at sufficiently large r_a. It is amazing to see that the behavior of $O^2_{\rm TT}$ is almost identical for both FQHSs and FCIs even though r_a is defined slightly differently. That is, $r_a = L_x/L_y$ and N_x/N_y for FQHSs and FCIs, respectively. Most importantly, the Tao-Thouless state is firmly established at $r_a \gtrsim N/2\pi\nu$, as expected from the previous argument based on the suppression of quantum fluctuations. This means that, for FCIs, the Tao-Thouless state can be obtained if $N_y \lesssim \sqrt{2\pi} \simeq 2.5066$, which is consistent with our numerical finding that $O^2_{\rm TT}$ is essentially unity for $N_y = 1$ and 2.

On the other hand, Fig. 4 shows that $O^2_{\rm TT}$ is vanishingly small at $r_a \simeq 1$, meaning that the 1/3-filled FCI is poorly represented by the Tao-Thouless state in the 2D bulk. For a better description of the 1/3-filled FCI in the 2D bulk, quantum fluctuations should be appropriately incorporated into the Tao-Thouless state, which actually amounts to the construction of the Chern-Laughlin state. Note that, with proper basis states, the Tao-Thouless state can be used to explicitly construct the Chern-Laughlin state in the disk geometry via the Jack polynomial method [12]. In this work, we take a different approach that can be applied to the torus geometry.

F. Quantum fluctuations

The Chern-Laughlin state can be constructed from the Laughlin state by using the one-to-one mapping between LL and WSL eigenstates. Concretely, the amplitude of the Chern-Laughlin state at the desired WSL eigenstate can be imported from that of the Laughlin state at the corresponding LL eigenstate.

There exists, however, a prerequisite for this import to work: the relative phase between different WSL eigenstates should be properly fixed so that they form a coherent basis set. While this can be done by using the previous gauge-fixing

method developed for maximally localized hybrid Wannier functions [9], here we use a method much more suited for WSL eigenstates, which are obtained numerically in this work by diagonalizing the Stark Hamiltonian. Specifically, our method is based on the topological property of WSL eigenstates by which they evolve continuously to each other by changing $k_\perp$ just as LL eigenstates do so by changing $k_{\rm LL}$. Note that this is merely the topological winding of WSL eigenstates shown in Fig. 3(a).

Mathematically, one can construct the coherent basis set of WSL eigenstates with proper gauge-fixing as follows:

$$\left|\phi^{\rm WSL}_{n,k_\perp}\right\rangle = e^{i\Theta_{n,k_\perp}}\left|\overline{\phi^{\rm WSL}_{n,k_\perp}}\right\rangle, \tag{17}$$

where $|\overline{\phi^{\rm WSL}_{n,k_\perp}}\rangle$ is the normalized WSL eigenstate under the particular gauge-fixing condition that $\overline{\phi^{\rm WSL}_{n,k_\perp}}(k_\parallel) = \langle k_\parallel|\overline{\phi^{\rm WSL}_{n,k_\perp}}\rangle$ is real at a certain value of $k_\parallel$, which should be carefully chosen to avoid any singularities of $\mathcal{A}_{\mathbf{k}}$ along the line of $(k_\parallel, k_\perp)$ with $k_\perp \in [0, 2\pi]$. The coherent phase, $\Theta_{n,k_\perp}$, can be determined by

$$\Theta_{n,k_\perp} = \int_0^{2\pi n+k_\perp} d\kappa \mathcal{A}^{\rm WSL}(\kappa), \tag{18}$$

where $\mathcal{A}^{\rm WSL}(\kappa) = \langle\overline{\phi^{\rm WSL}_{n,k'_\perp}}|i\partial_{k'_\perp}|\overline{\phi^{\rm WSL}_{n,k'_\perp}}\rangle|_{\kappa=2\pi n+k'_\perp}$ is the Berry connection of WSL eigenstates. As mentioned previously, with this coherent basis set of WSL eigenstates, the Chern-Laughlin state can be constructed by importing the amplitude of the Laughlin state at each LL eigenstate and attaching it to the corresponding WSL eigenstate.

Now, similar to the Tao-Thouless state, we compute the degeneracy-averaged square of overlap between three exact ground states of the triply degenerate GSM for the Coulomb interaction, $|\Psi^{\rm Coul}_{n=1,2,3}\rangle$, and the Chern-Laughlin state, $|\Psi^{\rm CL}_{n=1,2,3}\rangle$:

$$O^2_{\rm CL} = \frac{1}{3}\sum_{n,m=1}^{3}\left|\left\langle\Psi^{\rm CL}_n\middle|\Psi^{\rm Coul}_m\right\rangle\right|^2, \tag{19}$$

which should be sizable if quantum fluctuations are appropriately incorporated in the Chern-Laughlin state.

Figure 5 shows $O^2_{\rm CL}$ as a function of the Bloch frequency (which is proportional to the effective electric field strength) for various aspect ratios. Three features are worth noticing. First, $O^2_{\rm CL}$ is always maximized in the limit of large electric field strengths. This means that the exact Coulomb ground state is best described by the Chern-Laughlin state with maximally localized WSL eigenstates. Second, quantum fluctuations take up a dominant portion of the exact Coulomb ground state in the 2D bulk as shown by the huge increase from $O^2_{\rm TT}$ to $O^2_{\rm CL}$ in "2D Bulk" systems. The existence of such large quantum fluctuations indicates that the FCI is not a simple charge density wave state in the 2D bulk. Third, the maximum of $O^2_{\rm CL}$ is quite high not only in the thin torus limit, but also in the 2D bulk, proving that the exact Coulomb ground state is well described by the Chern-Laughlin state regardless of the aspect ratio.

Finally, we have confirmed that the Chern-Laughlin state provides an excellent description of the 1/3-filled FCI also for the nearest-neighbor interaction in the 2D bulk with basically the same level of overlap reported in previous studies [9].

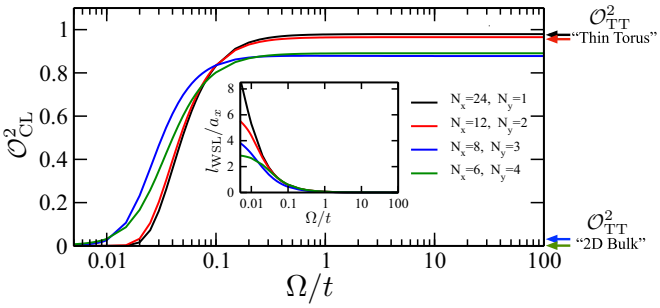

FIG. 5. Overlap between the 1/3-filled FCI and the Chern-Laughlin state in the checkerboard lattice model. The overlap is plotted in terms of the degeneracy-averaged square of overlap between three exact ground states of the triply degenerate GSM for the Coulomb interaction and the Chern-Laughlin state, $O^2_{\rm CL}$, in the 1/3-filled Chern flat band of the checkerboard lattice model as a function of the Bloch frequency in units of the nearest-neighbor hopping parameter, Ω/t. Specifically, different lines denote $O^2_{\rm CL}$ for the same site number, $N_s = N_x N_y = 24$, but different aspect ratios, $r_a = N_x/N_y$. The inset shows the wave-packet localization width of WSL eigenstates in units of the lattice constant along the x direction, $l_{\rm WSL}/a_x$, as a function of Ω/t, which can be computed as the standard deviation of the gauge-invariant position operator averaged over various WSL eigenstates. Color-coded arrows on the right frame of the figure indicate $O^2_{\rm TT}$ of the corresponding systems with various aspect ratios, which can be categorized as two groups, "Thin Torus" and "2D Bulk," depending on whether $O^2_{\rm CL}$ and $O^2_{\rm TT}$ are similar or not in the limit of large Ω/t.

IV. RESULTS FOR THE KAGOME LATTICE MODEL

In this section, we perform an analysis of $\mathcal{H}_{\rm CFB}$ via exact diagonalization for the kagome lattice model at 1/3 filling, mirroring what was done for the checkerboard lattice model.

A. Hybrid adiabatic path

Figure 6 shows a comparison between energy spectra of the nearest-neighbor and Coulomb interactions in the kagome lattice as a function of (N_x, N_y) for $N = 8$ and $N_s = 24$.

As one can see, the behavior of energy spectra is essentially the same as that in the checkerboard lattice model. Specifically, Figs. 6(a)–6(d) show that the triply degenerate GSM collapses if one takes the thin torus limit directly for the nearest-neighbor interaction. On the other hand, Figs. 6(e)–6(h) show that the triply degenerate GSM remains intact for the Coulomb interaction all the way to the thin torus limit.

Similar to what is done for the checkerboard lattice model, we investigate the adiabatic continuity of the triply degenerate GSM in the 2D bulk by deforming the electron-electron interaction from the nearest-neighbor to Coulomb interaction via $U(\lambda) = (1-\lambda)U^{\rm NN} + \lambda U^{\rm Coul}$. Figure 6(i) shows that the energy gap between the third and fourth lowest energies remains open as a function of λ in the 2D bulk, i.e., at $(N_x, N_y) = (6, 4)$, Again, the energy gap only closes at very small λ in the thin torus limit, i.e., $(N_x, N_y) = (24, 1)$, meaning that the Tao-Thouless state can also be obtained in the thin torus limit

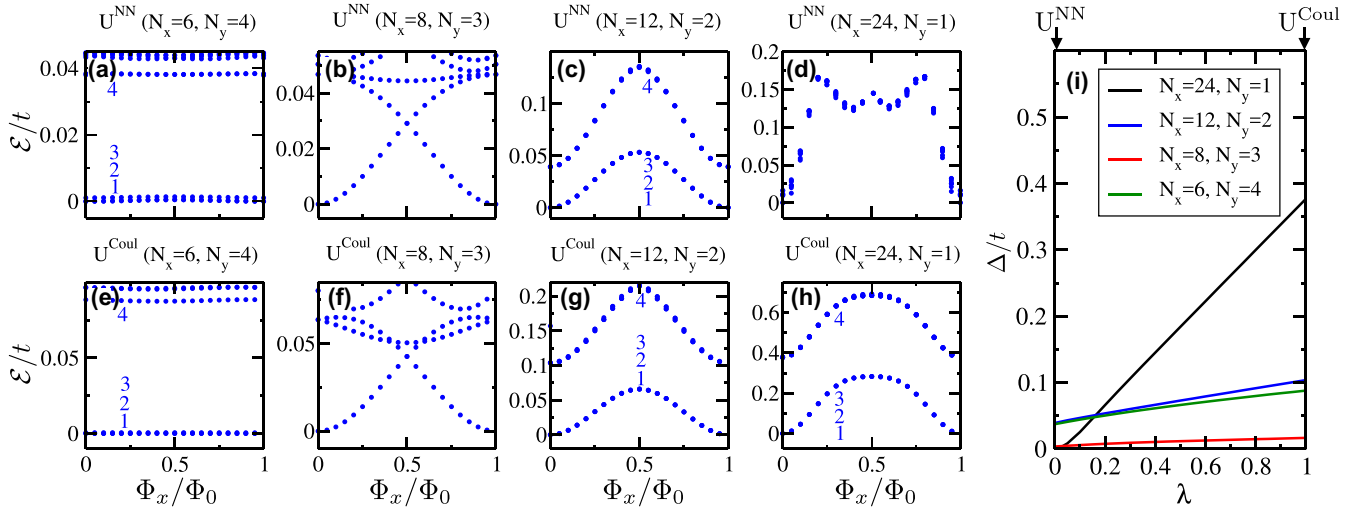

FIG. 6. Energy spectra of the nearest-neighbor and Coulomb interactions in the kagome lattice model. (a)–(d) Energy spectra of $U^{\rm NN}$ in the kagome lattice model as a function of Φ_x/Φ_0 for various values of (N_x, N_y). (e)–(h) Similar energy spectra of $U^{\rm Coul}$. (i) Energy gap, Δ, between the third and fourth lowest energies as a function of λ. All notations are similarly defined as in Fig. 1.

of the kagome lattice unless the electron-electron interaction is strictly of nearest-neighbor form.

B. Topological spectral flow

Similar to the corresponding case in the checkerboard lattice model, Figs. 6(b) and 6(f) show a clear verification of the topological spectral flow at $(N_x, N_y) = (8, 3)$ with the insertion of the test flux along the x direction. Again, at this aspect ratio, all three constituent ground states of the triply degenerate GSM occur in the same K_x, but different K_y, sectors.

To verify the topological spectral flow at other aspect ratios, we investigate how the three ground-state energies of the triply degenerate GSM change as a function of the test flux along the y direction. As expected, Fig. 7 shows that the topological spectral flow exists as a function of the test flux along the y direction for $(N_x, N_y) = (6, 4)$, $(12, 2)$, and $(24, 1)$. Again, here, the energy differences between three constituent ground states of the triply degenerate GSM are exceedingly small in comparison with those at $(N_x, N_y) = (8, 3)$.

C. Many-body Chern number

Similar to the checkerboard lattice model, the total many-body Chern number is also precisely quantized to be unity for the entire triply degenerate GSM of the Coulomb interaction at all possible aspect ratios in the kagome lattice model. Again, while not completely legitimate, the many-body Chern number can be evaluated for each constituent ground state of the triply degenerate GSM, which is confirmed to be $\mathcal{C}_{\rm MB} \simeq 0.33$, as expected.

D. Wannier-Stark ladder eigenstates

Figure 8(a) shows the topological winding of WSL eigenstates in the Chern flat band of the kagome lattice model with $(N_x, N_y) = (6, 6)$. With the Chern number $\mathcal{C} = 1$, here, the wave-packet center position of WSL eigenstates winds up monotonically as a function of k_y in the presence of the effective electric field applied along the x direction. Meanwhile, Fig. 8(b) shows that there is no such winding in the topologically trivial situation. This means that the one-to-one mapping between LL and WSL eigenstates can also be established for the Chern flat band of the kagome lattice model as well.

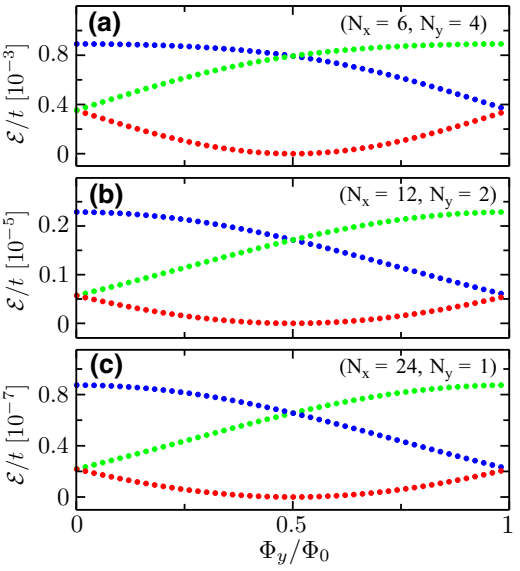

FIG. 7. Topological spectral flow of the triply degenerate GSM under the flux insertion along the y direction in the kagome lattice model. Similar to Fig. 2, three ground-state energies of the triply degenerate GSM for the Coulomb interaction are plotted as a function of Φ_y/Φ_0 for $(N_x, N_y) = (6, 4)$, $(12, 2)$, and $(24, 1)$ in (a), (b), and (c), respectively. All notations are similarly defined as in Fig. 2.

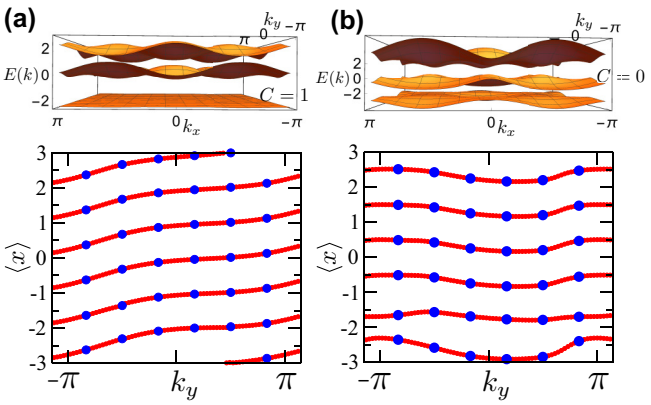

FIG. 8. Topological winding of WSL eigenstates in the kagome lattice model. Similar to Fig. 3, the effective electric field inducing WSL eigenstates is applied along the x direction. (a) Wave-packet center position $\langle x \rangle$ of WSL eigenstates as a function of k_y in the Chern flat band of the kagome lattice model, which is the bottom energy band indicated by the Chern number $\mathcal{C} = 1$ in the top panel. Topological winding with a positive slope confirms $\mathcal{C} = 1$. (b) Similar plot in the topologically trivial band, which is the middle energy band indicated by the Chern number $\mathcal{C} = 0$ in the top panel. As one can see, there is no winding. All notations are similarly defined as in Fig. 3. Also, here, $(N_x, N_y) = (6, 6)$.

E. Tao-Thouless state

Figure 9 shows the degeneracy-averaged square of overlap between three exact ground states of the triply degenerate GSM for the Coulomb interaction and the Tao-Thouless state, O^2_{TT}, in the 1/3-filled Chern flat band of the kagome lattice model as a function of r_a.

As one can see, the behavior of O^2_{TT} in the kagome lattice model is almost exactly the same as that in the checkerboard counterpart. Specifically, O^2_{TT} follows almost exactly the same curve of the similar overlap in the 1/3-filled FQHS, which is constructed in the torus geometry with oblique unit cells. Again, it is shown that O^2_{TT} is essentially unity at $r_a \gtrsim N/2\pi v$,

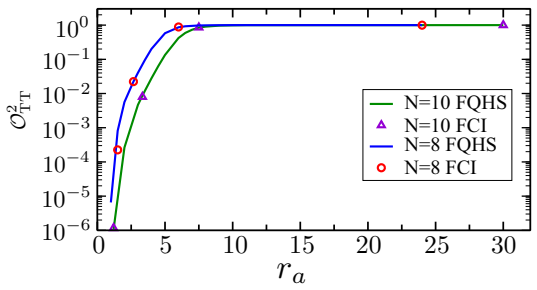

FIG. 9. Overlap between the 1/3-filled FCI and the Tao-Thouless state in the kagome lattice model. Similar to Fig. 4, open symbols denote the degeneracy-averaged square of overlap between three exact ground states of the triply degenerate GSM for the Coulomb interaction and the Tao-Thouless state, O^2_{TT}, in the 1/3-filled Chern flat band of the kagome lattice model as a function of $r_a = N_x/N_y$. Continuous lines denote the similar overlaps for the 1/3-filled FQHS. Note that FQHSs are constructed in the torus geometry with oblique unit cells, which match the shape of those in the kagome lattice. All notations are similarly defined as in Fig. 4.

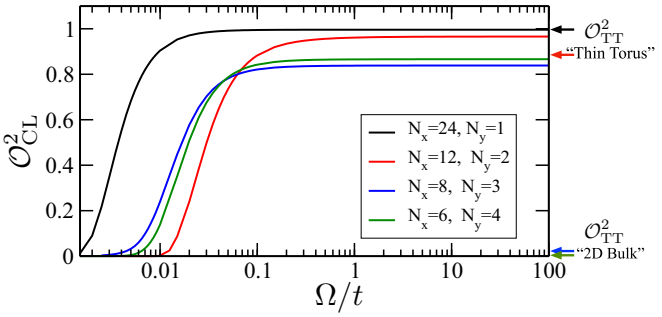

FIG. 10. Overlap between the 1/3-filled FCI and the Chern-Laughlin state in the kagome lattice model. Similar to Fig. 5, the overlap is plotted in terms of the degeneracy-averaged square of overlap between three exact ground states of the triply degenerate GSM for the Coulomb interaction and the Chern-Laughlin state, O^2_{CL}, in the 1/3-filled Chern flat band of the kagome lattice model as a function of Ω/t. All notations are similarly defined as in Fig. 5.

indicating that the Tao-Thouless state is firmly established at $N_y = 1$ and 2.

F. Quantum fluctuations

Figure 10 shows the degeneracy-averaged square of overlap between three exact ground states of the triply degenerate GSM for the Coulomb interaction and the Chern-Laughlin state, O^2_{CL}, in the 1/3-filled Chern flat band of the kagome lattice model as a function of Ω/t for various aspect ratios.

Here we observe essentially the same three features as those in the checkerboard lattice model. First, O^2_{CL} is always maximized in the limit of large Ω, meaning that the exact Coulomb ground state is best described by the Chern-Laughlin state with maximally localized WSL eigenstates. Second, quantum fluctuations take up a dominant portion of the exact Coulomb ground state in the 2D bulk. Third, regardless of the aspect ratio, the exact Coulomb ground state is well described by the Chern-Laughlin state, which can be constructed by incorporating appropriate quantum fluctuations into the Tao-Thouless state while maintaining the energy gap.

Finally, note that, similar to the checkerboard lattice model, the Chern-Laughlin state provides an excellent description of the 1/3-filled FCI also for the nearest-neighbor interaction in the 2D bulk of the kagome lattice model with basically the same level of the overlap reported in Ref. [9], while there are some small discrepancies. These discrepancies are mainly due to the fact that we have used a slightly different set of parameters for the Hamiltonian of the kagome lattice model from that in the previous study. We have chosen our set of parameters to make the energy dispersion of the Chern flat band as flat as possible rather than simply ignoring it.

V. DISCUSSION

The main purpose of our work is to propose both a theoretically precise and experimentally viable method to visualize the fractional topological order of the Chern-Laughlin state in the 1/3-filled Chern flat band and various FCIs at other general filling factors.

Theoretically, it is shown in our work that the 1/3-filled FCI can be adiabatically connected to the Tao-Thouless state via the hybrid adiabatic path of first deforming the electron-electron interaction from the nearest-neighbor to Coulomb interaction and then taking the thin torus limit. Similar to the usual CDW states, the Tao-Thouless state can be, in principle, directly detected in terms of its characteristic charge density patterns represented by $|100\cdots\rangle$, $|010\cdots\rangle$, and $|001\cdots\rangle$ with 1 and 0 denoting filled and empty WSL eigenstates, respectively, and ellipses denoting repeated patterns. A detection of the Tao-Thouless state would provide conclusive experimental evidence for the existence of the Chern-Laughlin state, which can be constructed by incorporating appropriate quantum fluctuations into the Tao-Thouless state.

Importantly, our work establishes the existence of an adiabatic path from the 1/3-filled FCI to the Tao-Thouless state by taking the thin torus limit in the same Hamiltonian with a fixed form of the electron-electron interaction, which can maintain the robust energy gap unless the electron-electron interaction is strictly of the nearest-neighbor form. Such an adiabatic path is different from those proposed in previous works [10,11], where the Hamiltonian itself is deformed by linearly mixing two different limiting forms of the Hamiltonian along the path. As elaborated below, our work opens up the exciting possibility of detecting the Tao-Thouless state in actual experiments.

Experimentally, a recent observation of FCIs in the MATBG [15] suggests that the Tao-Thouless state can actually be detected in an incommensurate double-walled carbon nanotube [40] made out of the MATBG, allowing charge-sensitive surface measurements such as scanning tunneling microscopy [41,42]. Note that the MATBG nanotube can act as the thin torus limit of Chern flat bands so long as it has up to two moiré unit cells along the tubular circumference.

Our method can be extended to other general FCIs corresponding to both Abelian and non-Abelian FQHSs. Regarding the Abelian states, root partition states are known for all the FQHSs belonging to the Jain sequence [31]. The existence of these root partition states can be investigated in the thin torus limit of Chern flat bands at their corresponding filling factors. In particular, it would be interesting to investigate if the Chern CF sea, the FCI analog of the CF sea, can arise in the half-filled Chern flat band.

Regarding the non-Abelian states, while there are many variations, perhaps the most important non-Abelian state would be the Moore-Read Pfaffian state [62–64]. Considering the possible application to topological quantum computation [65], it would be interesting to know if and how a lattice analog of the Moor-Read Pfaffian state can be realized in the half-filled Chern flat band, competing against the Chern CF sea.

Being the zero-energy ground state of the three-body repulsive interaction, the Moore-Read Pfaffian state is expected to have sextuply degenerate root partition states in the thin torus limit [31]: (i) two single-isolated-electron root partition states, $|1010\cdots\rangle$ and $|0101\cdots\rangle$, and (ii) four paired-electron root partition states, $|1100\cdots\rangle$, $|0110\cdots\rangle$, $|0011\cdots\rangle$, and $|1001\cdots\rangle$, with 1 and 0 denoting filled and empty WSL eigenstates, respectively, and ellipses denoting repeated patterns. Just like the Tao-Thouless state, a detection of these root partition states would provide conclusive experimental evidence for the existence of the Moore-Read Pfaffian state. A similar idea can be applied to other important non-Abelian states such as the Z_k parafermion states, which include the Read-Rezayi state at $k = 3$ [66].

At this point, it is important to ask if root partition states can always be obtained for general FCIs by simply taking the thin torus limit. While there is no guarantee, our work suggests that the answer to this question is likely to be positive. It is shown in our work that the overlap between the Tao-Thouless and the exact Coulomb ground states in the 1/3-filled Chern flat band behaves almost identically to that in the fractional quantum Hall counterpart as a function of the aspect ratio. This suggests that general FCIs can be adiabatically connected to their corresponding root partition states, so long as the electron-electron interaction is sufficiently long-ranged.

Finally, it is important to note that, while similar, the Tao-Thouless state and various other root partition states can be clearly distinguished from the usual CDW states via their characteristic topological property. That is to say, let us imagine a situation in which the magnetic flux is inserted along the tubular axis of the MATBG nanotube. With this insertion of the magnetic flux, root partition states are spatially translated along the tubular axis, which is actually nothing but the topological spectral flow in the thin torus limit, also known as the charge pumping. Specifically, there would be a spatial translation causing the cyclic interchange among $|100\cdots\rangle$, $|010\cdots\rangle$, and $|001\cdots\rangle$ for the Tao-Thouless state. By contrast, there would be no charge pumping for the usual CDW states.

ACKNOWLEDGMENTS

The authors are grateful to J. K. Jain and Y.-W. Son for insightful discussions. Also, the authors thank Center for Advanced Computation (CAC) at Korea Institute for Advanced Study (KIAS) for providing computing resources for this work. This work was supported in part by the KIAS Individual Grants, PG034303 (S.M.) and PG032303 (K.P.), and also by the National Research Foundation of Korea (NRF) funded by the Ministry of Science and ICT of the Korean Government, NRF-2021M3H3A1085208 (K.P.), which is jointly granted under the US-Korea Quantum Initiative by the U.S. Air Force Office of Scientific Research (AFOSR), FA2386-21-1-4081 (US PI: Vito Scarola).

APPENDIX A: TIGHT-BINDING MODEL HAMILTONIANS

We focus on two tight-binding model Hamiltonians to generate Chern flat bands: (i) H_{checker} for the checkerboard lattice [2] and (ii) H_{kagome} for the kagome lattice [3].

First, the tight-binding model Hamiltonian for the checkerboard lattice can be written as follows:

$$H_{\text{checker}} = \sum_{\mathbf{k}} (c^\dagger_{a\mathbf{k}} \;\; c^\dagger_{b\mathbf{k}}) H_{\mathbf{k}} \begin{pmatrix} c_{a\mathbf{k}} \\ c_{b\mathbf{k}} \end{pmatrix}, \tag{A1}$$

where

$$H_{\mathbf{k}} = -[(t_1' + t_2')(\cos k_x + \cos k_y) + 4t'' \cos k_x \cos k_y]I - 4t \cos\phi \cos\frac{k_x}{2}\cos\frac{k_y}{2}\sigma_x - 4t \sin\phi \sin\frac{k_x}{2}\sin\frac{k_y}{2}\sigma_y - [(t_1' - t_2')(\cos k_x - \cos k_y) + M]\sigma_z, \tag{A2}$$

where $c_{a\mathbf{k}}$ and $c_{b\mathbf{k}}$ are the electron annihilation operators at momentum $\mathbf{k}$ for a- and b-sublattices, respectively, I is the identity matrix, and $\sigma_{x,y,z}$ are the Pauli matrices. As written above, H_{checker} is not of the proper Bloch form, in which case the Chern number cannot be correctly computed. H_{checker} can be brought to a proper Bloch form via the gauge transformation of $c_{b\mathbf{k}} \to e^{-i(k_x-k_y)/2}c_{b\mathbf{k}}$ [7]. Finally, the value of M controls the transition between topologically trivial and nontrivial phases.

For the choice of parameters with $t = 1$, $t_1' = -t_2' = 1/(2+\sqrt{2})$, $t'' = 1/(2+2\sqrt{2})$, $\phi = \pi/4$, and $M = 0$, H_{checker} generates a gapped energy spectrum containing two energy bands with Chern numbers $C = \pm 1$. The upper energy band with $C = -1$ has a bandwidth of nearly $1/30$ of the band gap and thus can serve as a Chern flat band suitable for the realization of FCIs.

Second, the tight-binding model Hamiltonian for the kagome lattice can be written as follows:

$$H_{\text{kagome}} = \sum_{\mathbf{k}} (c_{a\mathbf{k}}^\dagger \;\; c_{b\mathbf{k}}^\dagger \;\; c_{c\mathbf{k}}^\dagger) H_{\mathbf{k}} \begin{pmatrix} c_{a\mathbf{k}} \\ c_{b\mathbf{k}} \\ c_{c\mathbf{k}} \end{pmatrix}, \tag{A3}$$

where

$$H_{\mathbf{k}} = \begin{pmatrix} 0 & h_{12}(\mathbf{k}) & h_{13}(\mathbf{k}) \\ h_{12}^*(\mathbf{k}) & 0 & h_{23}(\mathbf{k}) \\ h_{13}^*(\mathbf{k}) & h_{23}^*(\mathbf{k}) & 0 \end{pmatrix} \tag{A4}$$

with nonzero matrix elements of $H_{\mathbf{k}}$ given by

$$h_{12}(\mathbf{k}) = -2(t - i\lambda)\cos\frac{k_1}{2} - 2(t' + i\lambda')\cos\left(\frac{k_2}{2} + \frac{k_3}{2}\right),$$
$$h_{13}(\mathbf{k}) = -2(t + i\lambda)\cos\frac{k_2}{2} - 2(t' - i\lambda')\cos\left(\frac{k_3}{2} - \frac{k_1}{2}\right),$$
$$h_{23}(\mathbf{k}) = -2(t - i\lambda)\cos\frac{k_3}{2} - 2(t' + i\lambda')\cos\left(\frac{k_1}{2} + \frac{k_2}{2}\right), \tag{A5}$$

where $k_1 = k_x$, $k_2 = (k_x + \sqrt{3}k_y)/2$, and $k_3 = k_2 - k_1$. Similar to H_{checker}, H_{kagome} can be brought to a proper Bloch form via the gauge transformation of $c_{b\mathbf{k}} \to e^{-ik_1/2}c_{b\mathbf{k}}$ and $c_{c\mathbf{k}} \to e^{-ik_2/2}c_{c\mathbf{k}}$.

For the choice of parameters with $t = 1$, $t' = -0.3$, $\lambda = 0.28$, and $\lambda' = 0.2$, H_{kagome} generates a gapped energy spectrum containing three bands with Chern numbers $C = 1, 0, -1$. The bottom energy band with $C = 1$ has a bandwidth of nearly $1/52$ of the band gap against the middle energy band, serving as a Chern flat band suitable for the realization of FCIs.

APPENDIX B: PROJECTED INTERACTION MATRIX ELEMENTS

We begin by writing the projected electron-electron interaction operator in real space as follows:

$$\hat{U} = \frac{1}{2}\sum_{a,b}{\sum_{i,j}}' U(\mathbf{r}_i^a - \mathbf{r}_j^b)\mathcal{P}_{\text{CFB}}|\mathbf{r}_i^a, \mathbf{r}_j^b\rangle\langle\mathbf{r}_i^a, \mathbf{r}_j^b|\mathcal{P}_{\text{CFB}}, \tag{B1}$$

where a, b and i, j denote sublattice and unit cell indices, respectively. The prime indicates that the summation is restricted so that $i \neq j$ if $a = b$. The ket states $|\mathbf{r}_i^a\rangle$ and $|\mathbf{r}_i^a\rangle$ represent the position eigenstate at $\mathbf{r}_i^a$ and $\mathbf{r}_i^a$, respectively.

The projection operator to the Chern flat band, $\mathcal{P}_{\text{CFB}}$, modifies the position eigenstate at the a-sublattice as follows:

$$\mathcal{P}_{\text{CFB}}|\mathbf{r}_i^a\rangle = \sum_{\mathbf{k}} u_a^*(\mathbf{k})e^{i\theta_{\mathbf{k}}^a}e^{i\mathbf{k}\cdot\mathbf{r}_i^a}|\mathbf{k}\rangle, \tag{B2}$$

where $u_a(\mathbf{k})$ is the a-sublattice amplitude of the Bloch eigenstate with momentum $\mathbf{k}$ projected to the Chern flat band. The phase factor $e^{i\theta_{\mathbf{k}}^a}$ is due to the gauge transformation required to bring the Hamiltonian into a proper Bloch form. Projected position eigenstates can be similarly obtained for the b-sublattice.

Then, by using the momentum space representation of the projected position eigenstates in Eq. (B2), we can rewrite the projected electron-electron interaction operator in momentum space as follows:

$$\hat{U} = \sum_{\mathbf{k}_1,\mathbf{k}_2,\mathbf{k}_3,\mathbf{k}_4} \langle\mathbf{k}_1, \mathbf{k}_2|\hat{U}|\mathbf{k}_3, \mathbf{k}_4\rangle c_{\mathbf{k}_1}^\dagger c_{\mathbf{k}_2}^\dagger c_{\mathbf{k}_3}c_{\mathbf{k}_4}, \tag{B3}$$

with

$$\langle\mathbf{k}_1, \mathbf{k}_2|\hat{U}|\mathbf{k}_3, \mathbf{k}_4\rangle = \sum_{a,b}{\sum_{\delta\mathbf{r}}}' \delta_{\mathbf{k}_1+\mathbf{k}_2,\mathbf{k}_3+\mathbf{k}_4}U(\delta\mathbf{r})e^{i(\mathbf{k}_2-\mathbf{k}_4)\cdot\delta\mathbf{r}}e^{i(\theta_{\mathbf{k}_1}^a+\theta_{\mathbf{k}_2}^b-\theta_{\mathbf{k}_3}^a-\theta_{\mathbf{k}_4}^b)}u_a^*(\mathbf{k}_1)u_b^*(\mathbf{k}_2)u_a(\mathbf{k}_3)u_b(\mathbf{k}_4), \tag{B4}$$

where $\delta\mathbf{r} = \mathbf{r}_i^a - \mathbf{r}_j^b$ is the relative position vector and $U(\delta\mathbf{r})$ is the unprojected electron-electron interaction in the real space.

Finally, by using the momentum space representation of the projected electron-electron interaction matrix element in Eq. (B4), we can rewrite the projected electron-electron interaction operator in the WSL eigenstate space as follows:

$$\hat{U} = \sum_{\kappa_i,\kappa_j,\kappa_k,\kappa_l} \langle\kappa_i, \kappa_j|\hat{U}|\kappa_k, \kappa_l\rangle c_{\kappa_i}^\dagger c_{\kappa_j}^\dagger c_{\kappa_k}c_{\kappa_l}, \tag{B5}$$

with

$$\langle\kappa_i, \kappa_j|\hat{U}|\kappa_k, \kappa_l\rangle = \sum_{\mathbf{k}_1,\mathbf{k}_2,\mathbf{k}_3,\mathbf{k}_4} \langle\mathbf{k}_1, \mathbf{k}_2|\hat{U}|\mathbf{k}_3, \mathbf{k}_4\rangle\phi_{\kappa_i}^*(\mathbf{k}_1)\phi_{\kappa_j}^*(\mathbf{k}_2)\phi_{\kappa_k}(\mathbf{k}_3)\phi_{\kappa_l}(\mathbf{k}_4), \tag{B6}$$

where $\phi_\kappa(\mathbf{k})$ is related with WSL eigenstates via $\phi_\kappa(\mathbf{k}) = \phi^{\mathrm{WSL}}_{n,k_\perp}(k_\parallel)$ with $\kappa = 2\pi n + k_\perp$ (i.e., $k_\perp = \kappa \bmod 2\pi$) and $\mathbf{k} = k_\parallel \hat{e}_\parallel + k_\perp \hat{e}_\perp$ (i.e., $k_\parallel = \mathbf{k}\cdot\hat{e}_\parallel$). See the main text for the explicit definition of $\phi^{\mathrm{WSL}}_{n,k_\perp}(k_\parallel)$ in Eq. (13).

The physical form of the electron-electron interaction can be varied by changing $U(\delta\mathbf{r})$ in Eq. (B4). In the case of the nearest-neighbor interaction, $U(\delta\mathbf{r})$ is chosen to be $U^{\mathrm{NN}}(\delta\mathbf{r})$, which is nonzero only if $\delta\mathbf{r}$ is the relative position vector connecting between nearest-neighboring sites. In the case of the Coulomb interaction, $U(\delta\mathbf{r})$ is chosen to be $U^{\mathrm{Coul}}(\delta\mathbf{r})$, which is the usual $1/r$ potential except for an important modification due to repeated image charges induced by the periodic boundary condition.

APPENDIX C: EWALD SUMMATION FOR THE COULOMB INTERACTION

Following Bonsall and Maradudin [46], we can write the Coulomb interaction, $U^{\mathrm{Coul}}(\delta\mathbf{r})$, as follows:

$$U^{\mathrm{Coul}}(\delta\mathbf{r}) = \sum_{\mathbf{R}_l} \frac{e^2}{|\delta\mathbf{r}+\mathbf{R}_l|} = \frac{e^2}{\sqrt{a_c}} \sum_{\mathbf{G}\neq 0} e^{-i\mathbf{G}\cdot\delta\mathbf{r}} \varphi_{-\frac{1}{2}}\left(\frac{|\mathbf{G}|^2 a_c}{4\pi}\right) + \frac{e^2}{\sqrt{a_c}} \sum_{\mathbf{R}_l} \varphi_{-\frac{1}{2}}\left(\frac{\pi}{a_c}|\delta\mathbf{r}+\mathbf{R}_l|^2\right), \tag{C1}$$

where $\mathbf{R}_l = l_1 N_1 \hat{e}_1 + l_2 N_2 \hat{e}_2$, with $\hat{e}_1$ and $\hat{e}_2$ being the primitive lattice vectors of the supercell lattice, $\mathbf{G}$ is the corresponding reciprocal lattice vectors, and a_c is the area of the supercell. Finally, $\varphi_n(x) = \int_1^\infty dt\, t^n e^{-xt}$.

[1] D. C. Tsui, H. L. Stormer, and A. C. Gossard, Two-Dimensional Magnetotransport in the Extreme Quantum Limit, Phys. Rev. Lett. **48**, 1559 (1982).

[2] K. Sun, Z. Gu, H. Katsura, and S. D. Sarma, Nearly Flat-Bands with Nontrivial Topology, Phys. Rev. Lett. **106**, 236803 (2011).

[3] E. Tang, J.-W. Mei, and X.-G. Wen, High Temperature Fractional Quantum Hall States, Phys. Rev. Lett. **106**, 236802 (2011).

[4] D. N. Sheng, Z.-C. Gu, K. Sun, and L. Sheng, Fractional Quantum Hall Effect in the Absence of Landau Levels, Nat. Commun. **2**, 389 (2011).

[5] T. Neupert, L. Santos, C. Chamon, and C. Mudry, Fractional Quantum Hall States at Zero Magnetic Field, Phys. Rev. Lett. **106**, 236804 (2011).

[6] X.-L. Qi, Generic Wave-Function Description of Fractional Quantum Anomalous Hall States and Fractional Topological Insulators, Phys. Rev. Lett. **107**, 126803 (2011).

[7] N. Regnault and B. A. Bernevig, Fractional Chern Insulator, Phys. Rev. X **1**, 021014 (2011).

[8] Y.-L. Wu, B. A. Bernevig, and N. Regnault, Zoology of fractional Chern insulators, Phys. Rev. B **85**, 075116 (2012).

[9] Y.-L. Wu, N. Regnault, and B. A. Bernevig, Gauge-fixed Wannier wave functions for fractional topological insulators, Phys. Rev. B **86**, 085129 (2012).

[10] Y.-H. Wu, J. K. Jain, and K. Sun, Adiabatic continuity between Hofstadter and Chern insulator states, Phys. Rev. B **86**, 165129 (2012).

[11] T. Scaffidi and G. Möller, Adiabatic Continuation of Fractional Chern Insulators to Fractional Quantum Hall States, Phys. Rev. Lett. **109**, 246805 (2012).

[12] A. L. He, W. W. Luo, Y. F. Wang, and C. D. Gong, Wave functions for fractional Chern insulators in disk geometry, New J. Phys. **17**, 125005 (2015).

[13] B. Andrews, M. Mohan, and T. Neupert, Abelian topological order of $\nu = 2/5$ and 3/7 fractional quantum Hall states in lattice models, Phys. Rev. B **103**, 075132 (2021).

[14] B. Andrews, T. Neupert, and G. Möller, Stability, phase transitions, and numerical breakdown of fractional Chern insulators in higher Chern bands of the Hofstadter model, Phys. Rev. B **104**, 125107 (2021).

[15] Y. Xie, A. T. Pierce, J. M. Park, D. E. Parker, E. Khalaf, P. Ledwith, Y. Cao, S. H. Lee, S. Chen, P. R. Forrester, K. Watanabe, T. Taniguchi, A. Vishwanath, P. J. Herrero, and A. Yacoby, Fractional Chern insulators in magic-angle twisted bilayer graphene, Nature (London) **600**, 439 (2021).

[16] R. B. Laughlin, Anomalous Quantum Hall Effect: An Incompressible Quantum Fluid with Fractionally Charged Excitations, Phys. Rev. Lett. **50**, 1395 (1983).

[17] S. M. Girvin and A. H. MacDonald, Off-Diagonal Long-Range Order, Oblique Confinement, and the Fractional Quantum Hall Effect, Phys. Rev. Lett. **58**, 1252 (1987).

[18] N. Read, Order Parameter and Ginzburg-Landau Theory for the Fractional Quantum Hall Effect, Phys. Rev. Lett. **62**, 86 (1989).

[19] J. K. Jain, Composite-Fermion Approach for the Fractional Quantum Hall Effect, Phys. Rev. Lett. **63**, 199 (1989).

[20] Q. Niu, D. J. Thouless, and Y.-S. Wu, Quantized Hall conductance as a topological invariant, Phys. Rev. B **31**, 3372 (1985).

[21] D. J. Thouless, Level crossing and the fractional quantum Hall effect, Phys. Rev. B **40**, 12034(R) (1989).

[22] J.-S. Jeong, H. Lu, K. H. Lee, K. Hashimoto, S. B. Chung, and K. Park, Competing states for the fractional quantum Hall effect in the 1/3-filled second Landau level, Phys. Rev. B **96**, 125148 (2017).

[23] W. Faugno, T. Zhao, A. Balram, T. Jolicoeur, and J. K. Jain, Unconventional $\mathbb{Z}_n$ parton states at $\nu = 7/3$: Role of finite width, Phys. Rev. B **103**, 085303 (2021).

[24] A. A. Koulakov, M. M. Fogler, and B. I. Shklovskii, Charge Density Wave in Two-Dimensional Electron Liquid in Weak Magnetic Field, Phys. Rev. Lett. **76**, 499 (1996).

[25] M. M. Fogler, A. A. Koulakov, and B. I. Shklovskii, Ground state of a two-dimensional electron liquid in a weak magnetic field, Phys. Rev. B **54**, 1853 (1996).

[26] J. Xia, J. P. Eisenstein, L. N. Pfeiffer, and K. W. West, Evidence for a fractionally quantized Hall state with anisotropic longitudinal transport, Nat. Phys. **7**, 845 (2011).

[27] R. Tao and D. J. Thouless, Fractional quantization of Hall conductance, Phys. Rev. B **28**, 1142 (1983).

[28] E. H. Rezayi and F. D. M. Haldane, Laughlin state on stretched and squeezed cylinders and edge excitations in the quantum Hall effect, Phys. Rev. B **50**, 17199 (1994).

[29] D. H. Lee and J. M. Leinaas, Mott Insulators without Symmetry Breaking, Phys. Rev. Lett. **92**, 096401 (2004).
[30] A. Seidel, H. Fu, D. H. Lee, J. M. Leinaas, and J. Moore, Incompressible Quantum Liquids and New Conservation Laws, Phys. Rev. Lett. **95**, 266405 (2005).
[31] E. J. Bergholtz and A. Karlhede, Quantum Hall system in Tao-Thouless limit, Phys. Rev. B **77**, 155308 (2008).
[32] H. Li and F. D. M. Haldane, Entanglement Spectrum as a Generalization of Entanglement Entropy: Identification of Topological Order in Non-Abelian Fractional Quantum Hall Effect States, Phys. Rev. Lett. **101**, 010504 (2008).
[33] A. M. Läuchli, E. J. Bergholtz, J. Suorsa, and M. Haque, Disentangling Entanglement Spectra of Fractional Quantum Hall States on Torus Geometries, Phys. Rev. Lett. **104**, 156404 (2010).
[34] M. Hermanns, A. Chandran, N. Regnault, and B. A. Bernevig, Haldane statistics in the finite-size entanglement spectra of $1/m$ fractional quantum Hall states, Phys. Rev. B **84**, 121309(R) (2011)
[35] A. Chandran, M. Hermanns, N. Regnault, and B. A. Bernevig, Bulk-edge correspondence in entanglement spectra, Phys. Rev. B **84**, 205136 (2011).
[36] A. Sterdyniak, N. Regnault, and B. A. Bernevig, Extracting Excitations from Model State Entanglement, Phys. Rev. Lett. **106**, 100405 (2011)
[37] A. Sterdyniak, A. Chandran, N. Regnault, B. A. Bernevig, and Parsa Bonderson, Real-space entanglement spectrum of quantum Hall states, Phys. Rev. B **85**, 125308 (2012).
[38] R. Bistritzer and A. H. MacDonald, Moiré bands in twisted double-layer graphene, Proc. Natl. Acad. Sci. USA **108**, 12233 (2011).
[39] E. Y. Andrei and A. H. MacDonald, Graphene bilayers with a twist, Nat. Mater. **19**, 1265 (2020).
[40] M. Koshino, P. Moon, and Y.-W. Son, Incommensurate double-walled carbon nanotubes as one-dimensional moiré crystals, Phys. Rev. B **91**, 035405 (2015).
[41] Y. Jiang, X. Lai, K. Watanabe, T. Taniguchi, K. Haule, J. Mao, and E. Y. Andrei, Charge order and broken rotational symmetry in magic-angle twisted bilayer graphene, Nature (London) **573**, 91 (2019).
[42] C. Rubio-Verdú, S. Turkel, Y. Song, L. Klebl, R. Samajdar, M. S. Scheurer, J. W. F. Venderbos, K. Watanabe, T. Taniguchi, H. Ochoa, L. Xian, D. M. Kennes, R. M. Fernandes, Á. Rubio, and A. N. Pasupathy, Moiré nematic phase in twisted double bilayer graphene, Nat. Phys. **18**, 196 (2022).
[43] H. C. Po, L. Zou, T. Senthil, and A. Vishwanath, Faithful tight-binding models and fragile topology of magic-angle bilayer graphene, Phys. Rev. B **99**, 195455 (2019).
[44] B. A. Bernevig and N. Regnault, Thin-torus limit of fractional topological insulators, arXiv:1204.5682.
[45] D. Yoshioka, Ground state of the two-dimensional charged particles in a strong magnetic field and the fractional quantum Hall effect, Phys. Rev. B **29**, 6833 (1984).
[46] L. Bonsall and A. A. Maradudin, Some static properties of a two-dimensional Wigner crystal, Phys. Rev. B **15**, 1959 (1977).
[47] T. Fukui, Y. Hatsugai, and H. Suzuki, Chern numbers in discretized brillouin zone: Efficient method of computing (spin) hall conductances, J. Phys. Soc. Jpn. **74**, 1674 (2005).
[48] K. Kudo, H. Watanabe, T. Kariyado, and Y. Hatsugai, Many-Body Chern Number without Integration, Phys. Rev. Lett. **122**, 146601 (2019).
[49] E. E. Mendez, F. Agulló-Rueda, and J. M. Hong, Stark Localization in GaAs-GaAlAs Superlattices under an Electric Field, Phys. Rev. Lett. **60**, 2426 (1988).
[50] P. Voisin, J. Bleuse, C. Bouche, S. Gaillard, C. Alibert, and A. Regreny, Observation of the Wannier-Stark Quantization in a Semiconductor Superlattice, Phys. Rev. Lett. **61**, 1639 (1988).
[51] S. R. Wilkinson, C. F. Bharucha, K. W. Madison, Q. Niu, and M. G. Raizen, Observation of Atomic Wannier-Stark Ladders in an Accelerating Optical Potential, Phys. Rev. Lett. **76**, 4512 (1996).
[52] M. Ben Dahan, E. Peik, J. Reichel, Y. Castin, and C. Salomon, Bloch Oscillations of Atoms in an Optical Potential, Phys. Rev. Lett. **76**, 4508 (1996).
[53] A. Wacker, Semiconductor superlattices: A model system for nonlinear transport, Phys. Rep. **357**, 1 (2002).
[54] M. Glück, A. R. Kolovsky, and H. J. Korsch, Wannier-Stark resonances in optical and semiconductor superlattices, Phys. Rep. **366**, 103 (2002).
[55] S. Y. Kruchinin, F. Krausz, and V. Yakovlev, Colloquium: Strong-field phenomena in periodic systems, Rev. Mod. Phys. **90**, 021002 (2018).
[56] W.-R. Lee and K. Park, Direct manifestation of topological order in the winding number of the Wannier-Stark ladder, Phys. Rev. B **92**, 195144 (2015).
[57] J. Zak, Berry's Phase for Energy Bands in Solids, Phys. Rev. Lett. **62**, 2747 (1989).
[58] R. D. King-Smith and D. Vanderbilt, Theory of polarization of crystalline solids, Phys. Rev. B **47**, 1651 (1993).
[59] R. Resta, Quantum-Mechanical Position Operator in Extended Systems, Phys. Rev. Lett. **80**, 1800 (1998).
[60] F. D. M. Haldane and E. H. Rezayi, Periodic Laughlin-Jastrow wave functions for the fractional quantized Hall effect, Phys. Rev. B **31**, 2529 (1985).
[61] K. W. Kim, W.-R. Lee, Y. B. Kim, and K. Park, Surface to bulk Fermi arcs via Weyl nodes as topological defects, Nat. Commun. **7**, 13489 (2016).
[62] G. Moore and N. Read, Nonabelions in the fractional quantum Hall effect, Nucl. Phys. B **360**, 362 (1991).
[63] M. Greiter, X.-G. Wen, and F. Wilczek, Paired Hall State at Half Filling, Phys. Rev. Lett. **66**, 3205 (1991).
[64] K. Park, V. Melik-Alaverdian, N. E. Bonesteel, and J. K. Jain, Possibility of p-wave pairing of composite fermions at $\nu = 1/2$, Phys. Rev. B **58**, R10167(R) (1998).
[65] C. Nayak, S. H. Simon, A. Stern, M. Freedman, and S. Das Sarma, Non-Abelian anyons and topological quantum computation, Rev. Mod. Phys. **80**, 1083 (2008).
[66] N. Read and E. Rezayi, Beyond paired quantum Hall states: Parafermions and incompressible states in the first excited Landau level, Phys. Rev. B **59**, 8084 (1999).